Terahertz photonic crystal quantum cascade lasers

Hua Zhang[1*], L. Andrea Dunbar[1†], Giacomo Scalari[2], Romuald Houdré[1*] and Jérôme Faist[2]

[1]*Institut de Photonique et Electronique Quantique, Ecole Polytechnique Fédérale de Lausanne (EPFL), Station 3, Lausanne, CH-1015, Switzerland.*
[2]*Institut für Quantenelektronik, Eidgenössische Techniche Hochshule Zürich (ETHZ), Zürich, CH-8072, Switzerland.*
[†]*Now with Centre Suisse d'Electronique et de Microtechnique SA, Neuchâtel, CH-2002, Switzerland.*
[*]*Corresponding authors: hua.zhang@epfl.ch; romuald.houdre@epfl.ch*

Abstract: We combine photonic crystal and quantum cascade band engineering to create an in-plane laser at terahertz frequency. We demonstrate that such photonic crystal lasers strongly improve the performances of terahertz quantum cascade material in terms of threshold current, waveguide losses, emission mode selection, tunability and maximum operation temperature. The laser operates in a slow-light regime between the M saddle point and K band-edge in reciprocal lattice. Coarse frequency control of half of a terahertz is achieved by lithographically tuning the photonic crystal period. Thanks to field assisted gain shift and cavity pulling, the single mode emission is continuously tuned over 30 GHz.

OCIS codes: (130.3120) Integrated Optics; (130.5296) Photonic crystal waveguides; (130.0250) Optoelectronics; (140.3490) Lasers distributed-feedback; (140.5960) Semiconductor Lasers; (230.5590) Quantum Well Devices; (230.5298) Photonic crystals; (260.3090) Infrared, far.

References and links

1. J. Faist, F. Capasso, D. L. Sivco, C. Sirtori, A. L. Hutchinson, and A. Y. Cho, "Quantum cascade laser," Science **264**, 553-556 (1994).
2. B. S. Williams, "Terahertz quantum-cascade lasers," Nat. Photonics **1**, 517-525 (2007).
3. R. Kohler, A. Tredicucci, F. Beltram, H. E. Beere, E. H. Linfield, A. G. Davies, D. A. Ritchie, R. C. Iotti, and F. Rossi, "Terahertz semiconductor-heterostructure laser," Nature **417**, 156-159 (2002).
4. B. S. Williams, S. Kumar, Q. Hu, and J. L. Reno, "Operation of terahertz quantum-cascade lasers at 164 K in pulsed mode and at 117 K in continuous-wave mode," Opt. Express **13**, 3331-3339 (2005).
5. L. Mahler, R. Kohler, A. Tredicucci, F. Beltram, H. E. Beere, E. H. Linfield, D. A. Ritchie, and A. G. Davies, "Single-mode operation of terahertz quantum cascade lasers with distributed feedback resonators," Appl. Phys. Lett. **84**, 5446-5448 (2004).
6. L. Ajili, J. Faist, H. Beere, D. Ritchie, G. Davies, and E. Linfield, "Loss-coupled distributed feedback far-infrared quantum cascade lasers," Electron. Lett. **41**, 419-421 (2005).
7. S. Kumar, B. S. Williams, Q. Qin, A. W. M. Lee, Q. Hu, and J. L. Reno, "Surface-emitting distributed feedback terahertz quantum-cascade lasers in metal-metal waveguides," Opt. Express **15,** 113-128 (2007).
8. O. Demichel, L. Mahler, T. Losco, C. Mauro, R. Green, J. H. Xu, A. Tredicucci, F. Beltram, H. E. Beere, D. A. Ritchie, and V. Tamosiunas, "Surface plasmon photonic structures in terahertz quantum cascade lasers," Opt. Express **14**, 5335-5345 (2006).
9. L. A. Dunbar, R. Houdre, G. Scalari, L. Sirigu, M. Giovannini, and J. Faist, "Small optical volume terahertz emitting microdisk quantum cascade lasers," Appl. Phys. Lett. **90**, 141114 (2007).
10. D. W. Prather, S. Y. Shi, J. Murakowski, G. J. Schneider, A. Sharkawy, C. H. Chen, and B. L. Miao, "Photonic crystal structures and applications: Perspective, overview, and development," IEEE J. Sel. Top. Quantum Electron. **12**, 1416-1437 (2006).
11. O. Painter, R. K. Lee, A. Scherer, A. Yariv, J. D. O'Brien, P. D. Dapkus, and I. Kim, "Two-dimensional photonic band-gap defect mode laser," Science **284**, 1819-1821 (1999).
12. H. G. Park, S. H. Kim, S. H. Kwon, Y. G. Ju, J. K. Yang, J. H. Baek, S. B. Kim, and Y. H. Lee, "Electrically driven single-cell photonic crystal laser," Science **305**, 1444-1447 (2004).

#88988 - $15.00 USD Received 29 Oct 2007; revised 29 Nov 2007; accepted 29 Nov 2007; published 4 Dec 2007

13. R. Colombelli, K. Srinivasan, M. Troccoli, O. Painter, C. F. Gmachl, D. M. Tennant, A. M. Sergent, D. L. Sivco, A. Y. Cho, and F. Capasso, "Quantum cascade surface-emitting photonic crystal laser," Science **302**, 1374-1377 (2003).
14. J. P. Dowling, M. Scalora, M. J. Bloemer, and C. M. Bowden, "The Photonic Band-Edge Laser - a New Approach to Gain Enhancement," J. Appl. Phys. **75**, 1896-1899 (1994).
15. M. Meier, A. Mekis, A. Dodabalapur, A. Timko, R. E. Slusher, J. D. Joannopoulos, and O. Nalamasu, "Laser action from two-dimensional distributed feedback in photonic crystals," Appl. Phys. Lett. **74**, 7-9 (1999).
16. H. Y. Ryu, S. H. Kwon, Y. J. Lee, Y. H. Lee, and J. S. Kim, "Very-low-threshold photonic band-edge lasers from free-standing triangular photonic crystal slabs," Appl. Phys. Lett. **80**, 3476-3478 (2002).
17. M. Bahriz, V. Moreau, R. Colombelli, O. Crisafulli, and O. Painter, "Design of mid-IR and THz quantum cascade laser cavities with complete TM photonic bandgap," Opt. Express **15**, 5948-5965 (2007).
18. K. Inoue, M. Sasada, J. Kawamata, K. Sakoda, and J. W. Haus, "A two-dimensional photonic crystal laser," Jpn. J. Appl. Phys. Part 2-Letters **38,** L157-L159 (1999).
19. M. Ibanescu, E. J. Reed, and J. D. Joannopoulos, "Enhanced photonic band-gap confinement via van hove saddle point singularities," Phys. Rev. Lett. **96**, 033904 (2006).
20. S. Nojima, "Optical-gain enhancement in two-dimensional active photonic crystals," J. Appl. Phys. **90**, 545-551 (2001).
21. L. A. Dunbar, V. Moreau, R. Ferrini, R. Houdre, L. Sirigu, G. Scalari, M. Giovannini, N. Hoyler, and J. Faist, "Design, fabrication and optical characterisation of quantum cascade lasers at terahertz frequencies using photonic crystal reflectors," Opt. Express **13**, 8960-8968 (2005).
22. A. Benz, G. Fasching, C. Deutsch, A. M. Andrews, K. Unterrainer, P. Klang, W. Schrenk, and G. Strasser, "Terahertz photonic crystal resonators in double-metal waveguides," Opt. Express **15**, 12418-12424 (2007).
23. B. S. Williams, S. Kumar, H. Callebaut, Q. Hu, and J. L. Reno, "Terahertz quantum-cascade laser at lambda approximate to 100 μm using metal waveguide for mode confinement," Appl. Phys. Lett. **83**, 2124-2126 (2003).
24. S. Kohen, B. S. Williams, and Q. Hu, "Electromagnetic modeling of terahertz quantum cascade laser waveguides and resonators," J. Appl. Phys. **97**, 053106 (2005).
25. G. Scalari, N. Hoyler, M. Giovannini, and J. Faist, "Terahertz bound-to-continuum quantum-cascade lasers based on optical-phonon scattering extraction," Appl. Phys. Lett. **86**, 181101 (2005).
26. C. Walther, G. Scalari, J. Faist, H. Beere, and D. Ritchie, "Low frequency terahertz quantum cascade laser operating from 1.6 to 1.8 THz," Appl. Phys. Lett. **89**, 231121 (2006).

1. Introduction

Quantum Cascade Lasers (QCLs) [1,2] have attracted interest as the leading compact coherent semiconductor source in Terahertz (THz) frequency regime (1-10 THz, 30-300 μm) [3]. Applications include spectroscopy, imaging, sensing and environmental monitoring. One key challenge has been the design and fabrication of devices with a controlled single mode operation and a high operation temperature. The best value for the latter is still 164 K [4], achieved in a multimode Fabry-Pérot (FP) device. Although very good progress has been realized in the achievement of controlled single mode operation using distributed feedback (DFB) structures with either in-plane [5,6] surface emission [7,8], or a circular micro-cavity [9], such frequency control was accompanied by lower maximum operating temperature [7]. In addition, the electrical tunability of the DFB QCL remains small, in the range of 4 GHz [7].

Photonic crystal (PhC) band engineering has been shown to be an alternative method to control the emitting properties of conventional semiconductor lasers at Near-Infrared (NIR) and telecommunication wavelengths [10]. Extremely low thresholds under optical pumping have been achieved in so-called membrane structures [11], however, room temperature operation, with performance under electrical injection matching those of a conventional DFB lasers remains a challenge [12]. PhC lasers were reported in two forms, one is the photonic bandgap (PBG) defect mode laser [11,13] based on resonant cavity mode, the other is the PhC DFB type laser, either one (1D) or two-dimensional (2D) [14-17]. Close to band-edge, low group velocity (v_g) is responsible for a significant gain enhancement, proportional to the group index (n_g) [18]. Lasing oscillation can also occur at Van Hove singularities, for example at the M saddle point [15,19]. It was theoretically predicted that 2D PhC DFB gain enhancement is larger than in 1D DFB [20]. Fortunately, THz cascade structures are extremely well suited for their use in PhC structures, e.g., using PhC as external frequency selectors for FP cavity lasers [21] or hexagonal cavity lasers [22]. The double plasmon or

#88988 - $15.00 USD Received 29 Oct 2007; revised 29 Nov 2007; accepted 29 Nov 2007; published 4 Dec 2007

metal-metal waveguide [23], in which the TM polarized light is confined in the active region between two metallic layers, enables the fabrication of pillar structures possessing a complete PBG with no out of plane losses, as shown in Fig. 1. The same metallic layers can also provide the contacts for electrical injection.

We show here that such a structure provides, along with a spectral control of the emitted light, lower losses and a higher operating temperature than a state of the art device fabricated with a FP cavity. Vertical confinement is achieved with double plasmon waveguide structures [24]. Our device consists of an active region, patterned into a triangular lattice of pillars, created from the high refractive index semiconductor QCL gain material [Fig. 1(a)] embedded and planarized in benzocyclobutene (BCB) [Fig. 1(b)]. At the PhC band-edge, the structures act as pure 2D DFB resonators and thus provide the necessary feedback for lasing. The THz PhC QCL has a complete PBG for TM-polarized light with flat-bands over a large domain in k-space and low-loss band-edge states, and does not rely on defect modes and external mirrors. However, the double plasmon waveguide generates a large impedance mode mismatch that also generates reflection at the tile boundaries [Fig. 1(b)]. Several different lengths (from 600μm down to 100 μm) rectangular top contacts are used [Fig. 1(c)].

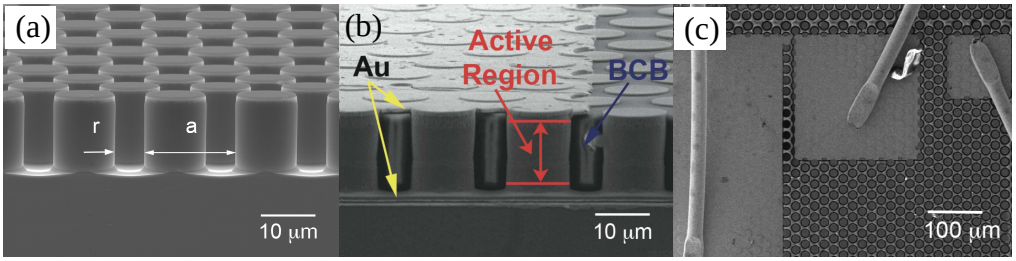

Fig. 1. Scanning Electron Microscope (SEM) images of THz PhC lasers. a, Cross-section SEM image of PhC pillars after dry etch, showing their high verticality and side-wall smoothness (~15.5 μm). b, Side view SEM image of double metal configuration bounding the PhC pillars which are surrounded by BCB. c, Top view SEM image of PhC tile lasers (lengths of square top contacts are 600 μm, 200 μm and 100 μm) with 25 μm diameter bonded gold wire.

2. Design, growth and fabrication

The Plane Wave Expansion (PWE) method was used to model the planar PhC as a 2D system to calculate the in-plane band structure for TM-polarized light. The real parts of the effective refractive indices are $n_{eff,QCL}$=3.53 and $n_{eff,BCB}$=1.9 for the double plasmon waveguide with QCL and BCB core, respectively. Figure 2(a) shows the overlap between the dispersion curve of the PhC structure and the QC material gain bandwidth (77~94 μm, 13.18~16.1 meV), which, for such intersubband transitions, is assumed to be identical to the spontaneous emission (SE) bandwidth. All quantities are plotted in reduced units, u=a/λ for the energy scale and k=k/(2π/a) for the wavevector, where 'a' is the lattice constant. By scanning 'a' from 14 μm to 23 μm (with 1 μm step size), the first PBG can be fully covered. 2D Finite-Element-Method (FEM) simulation with reflecting boundary condition finds a large number of resonance modes as a consequence of v_g reduction over an extended region of k space between M and K energies. The simulation confirms that the mode spacing is inversely proportional to the size of the PhC tile. The overlap between the calculated peak SE range and the band energy between M and K singularities in Fig. 2(a) indicates that our PhC tile QCLs with a values between 16 μm and 18 μm are in the optimum configuration for lasing, because the optical modes are mainly localized in the gain material (dielectric band) and the gain enhancement is maximum in the flat-band region.

The 120 periods of GaAs/$Al_{0.15}Ga_{0.85}As$ active layer is grown by Molecular Beam Epitaxy (MBE) on a semi-insulating GaAs substrate, its energy band diagram investigated here is similar to that described in Ref. [25]. After the wafer-wafer bonding forming the lower

#88988 - $15.00 USD Received 29 Oct 2007; revised 29 Nov 2007; accepted 29 Nov 2007; published 4 Dec 2007

surface plasmon layer, the PhC pattern was defined by photolithography and the sample was etched through completely [Fig. 1(a)]. Smooth and vertical sidewalls across the entire active region were achieved to reduce the scattering loss. BCB planarization technique on etched structures enables lithographic freedom of depositing top contacts [Fig. 1(b)], which also act as upper surface plasmon layer [Fig. 1(c)]. Unlike hole type PhC QCL devices [13], planarization with BCB eliminates the risks of device short circuit and metal contaminated mode perturbation, and provides ultimate freedom on the surface plasmon patterns. Details on the Electro-Luminescence (EL) spectra measurements, and light-current-voltage (L/I/V) curves against temperature in both pulsed and Continuous-Wave (CW) conditions are given in the annexe section.

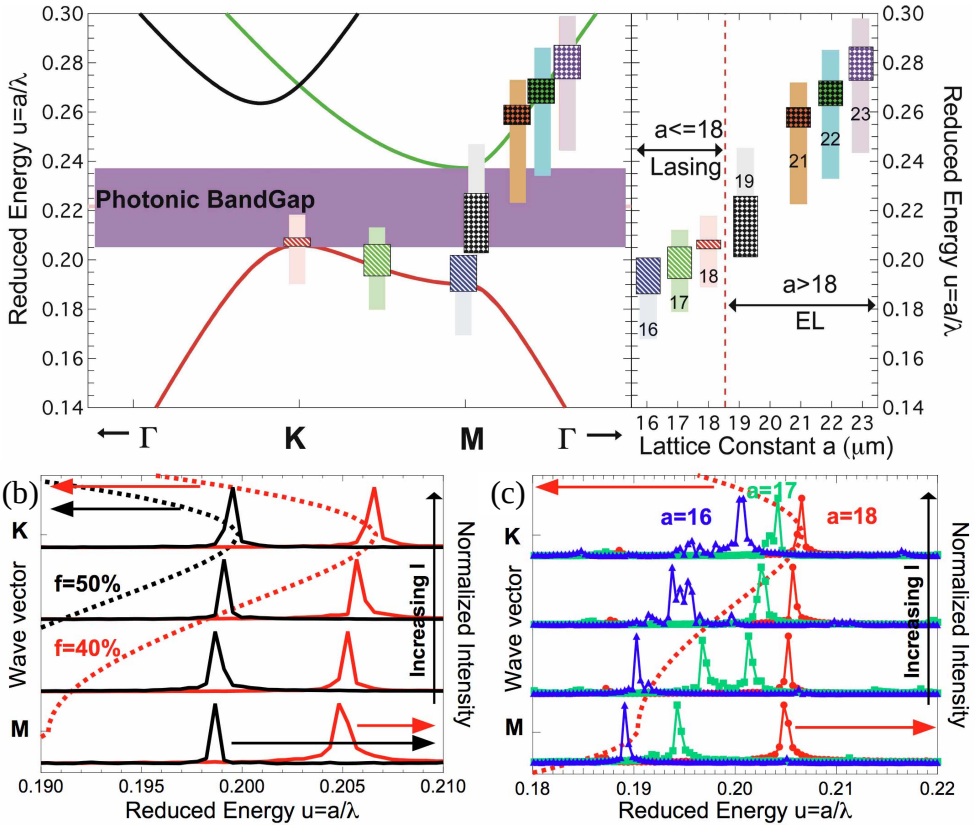

Fig. 2. Superimposition of material gain and experimentally measured spontaneous and lasing spectra emission ranges onto PhC dispersion curve and lasing emission spectra. a, Left panel shows the material gain range and measured emission spectra range superimposed onto PhC dispersion curve. Right panel shows the material gain and experimentally measured emission spectra range in reduced energy scale. Solid curves represent the PhC dispersion band diagram; wide patterned blocks represent the ranges of the observed lasers at a=16, 17 and 18 μm, or spontaneous emission at a=19, 21, 22 and 23 μm. Narrow rectangular blocks represent material gain. b, Left hand axis: black and red dashed lines represent the simulated PhC first bands for f=50% and 40% between M and K points respectively. Right hand axis: lasing spectra (solid curves) of same lattice constant a=18 μm at different 'f' 50% (black) and 40% (red). A 0.81% (30GHz) continuously dynamic single mode tuning is observed from f=40% curves. c, Left hand axis: Red dashed curve represents the simulated PhC first band of f=40% between M and K points. Right hand axis: Lasing spectra (solid curves) of f=40% at a=16(blue), 17(green) and 18 μm (red). A coarse lithographic tuning range of 14.6% (450GHz) is clearly shown.

#88988 - $15.00 USD Received 29 Oct 2007; revised 29 Nov 2007; accepted 29 Nov 2007; published 4 Dec 2007

3. Measurement results and discussion

The material gain (rectangular blocks) is superimposed onto the PhC dispersion curve of Fig. 2(a). Patterned blocks show the ranges of the experimentally observed laser or spontaneous emission. The a=18 μm spectra [Fig. 2(b)] at pillar filling factor 'f' 40% and 50% agree excellently with the corresponding calculated K band-edge, and a=16 μm spectra [Fig. 2(c)] under low current density correspond to the M point. The transition from M saddle point lasing (a=16 μm) to K band-edge lasing (a=18 μm) agrees with the theoretical expectation. The PhC tile QCLs emit predominantly in single mode, except under high injection current. The mode hopping at a=17 and 16 μm [Fig. 2(c)] is caused by the blue shifts of the material gain due to the diagonal nature of the bound to continuum transition. The drift continues until the next band-edge point (K) is reached. Note, however, that dispersion along the MK path remains flat and slow light gain enhancement still occurs. For the same lattice constant, PhC lasers with difference size of top contacts show very similar single mode spectral behaviour at localized M or K position, corroborating the fact that our PhC tile QCLs are lasing as 2D-DFB lasers, which lock in frequencies at the saddle point M and band-edge K. The smallest laser is only 11 periods long (~2.2 λ). No lasing behaviour was observed for the 100 μm long square laser, due to its small size (<5 periods), which cannot supply sufficient gain enhancement.

As can be seen in Fig. 2(b), these spectra show that due to cavity pulling the laser emission gradually shifts to higher energies with increasing current density. Note that relying on a cavity pulling effect by the field induced gain shift, the single mode emission can be dynamically and continuously tuned by a value as large as 30 GHz (0.85%), when the lasing frequency approaches the PhC band-edge (a=18 μm). The shift of the observed spectra from M to K points in Fig. 2(c) corresponds to an emission tuning in reduced energy scale '*u*' between 0.189 ~ 0.201 (3.55 THz to 3.77 THz) and 0.195 ~ 0.204 (3.43 THz to 3.60 THz) for a=16 and 17 μm, respectively. There is a total multimode coarse dynamic tuning range of 220 GHz (6.2%) by varying the injection current to change the properties of QC material, or 450 GHz (14.6%) lithographic tuning range by varying 'a' values to change the properties of PhC. Emission bandwidth of larger lattice constant tiles (19 μm<a<23 μm) either overlap the PBG frequencies or the air band whose modes have a limited spatial overlap with the QC material. Consequently only EL was observed. No lasing behaviour at a=14 and 15 μm is observed, due to the fact that there is no spectral overlap between the material gain range and the lowest M band singularity.

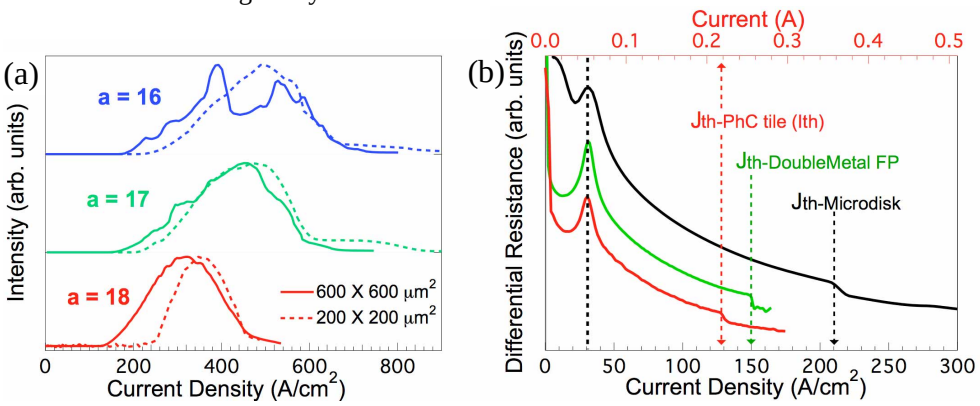

Fig. 3. Comparison of L/I curves of PhC tile lasers at different lattice constants and differential resistances. a, L/I characterization of PhC tile lasers at different lattice constants *a*=16(blue), 17(green) and 18(red) μm under pulsed condition (pulse=200 ns, duty cycle=1.3%). Solid lines represent the 600x600 μm² tile lasers, and dashed curves represent the 200x200 μm² tile lasers. b, Differential resistance versus current density under CW measurement for PhC tile laser (a=17 μm, red, bottom and top axis), double plasmon FP laser (1400x80 μm², green, bottom axis) and micro-disk laser (radius=50 μm, black, bottom axis), the PhC laser has the lowest threshold current density among the others.

#88988 - $15.00 USD Received 29 Oct 2007; revised 29 Nov 2007; accepted 29 Nov 2007; published 4 Dec 2007

Figure 3(a) illustrates the trend of the light-current (L/I) curves versus lattice constants. The increase of 'a' shows a concomitant decrease of the threshold current, due to the strongest overlap between the material gain peak and the optical mode energy at K band-edge for a=18 μm; this also results in its narrowest dynamic range, because the gain spectrum can only be shifted into the PBG where no modes can exist. In contrast, the optical mode frequency of smaller 'a' lasers (e.g. a=16 μm) have the potential to span a longer distance between MK path in the wave vector space, and to interact more with the material gain along its blue shifting, thereby giving it broader dynamic ranges.

It is difficult to obtain the threshold current density for devices based on electrically pumped PhCs precisely and directly, because of the uncertainties on calculating the surface area of the laser and the current spreading [13]. In our case, we circumvent this problem by analysing the miniband electronic transport of the lasing devices. Since all the devices tested show CW operation, we can precisely assess the threshold current density for the PhC tile QCL structures by inspecting the CW electronic transport characteristics of the devices and compare it to references FP and micro-disk laser, whose injection surface is precisely known. As widely used in electronic transport spectroscopy, we report in Fig. 3(b) a plot of the differential resistance dV/dI versus injected current at 10 K for a PhC tile QCL (a=17 μm), for a micro-disk laser (50 μm radius) and for a double plasmon FP laser fabricated with the same epilayer (N306). We can use the first prominent peaks in the differential resistance (at J=31 A/cm^2) for all samples for relative calibration and comparison. All peaks occur at the same current density, as they are the consequences of misalignment of the injector states from the lower miniband edge [3] state. Note that we defined the current density as the current divided by the cross section of active material, not the pad area, and therefore the "apparent" current density that would for example determine the thermal properties of the device are even lower. In this way current density directly quantifies the excitation of the active material itself and can be used to compare PhC and non-PhC lasers. The lasing threshold is deduced from the discontinuity in the differential resistance due to the onset of stimulated emission. The threshold current density for this tile PhC QCL sample is 128 A/cm^2 which shows a 17 % reduction compared to double metal FP laser, and 41% reduction compared to micro-disk laser.

Threshold reduction in lasers are usually achieved by reducing the relative weight of the out-coupling losses, either with the use of high reflectivity out-coupler or with an increase of the active region area. Similarly, the threshold reduction in band edge PhC lasers is achieved thanks to an enhancement of the modal gain within the crystal, or, equivalently, a reduction of the out-coupling losses. It is remarkable that, in opposition to a regular FP laser, this is achieved while reducing the volume of the active material, consequently reducing even more the threshold current. Comparison of a PhC tile laser with a FP laser of identical size (250x400 μm^2 and 1170x100 μm^2 for PhC and FP laser, respectively) shows a moderate reduction of the threshold current density from 155 to 145 A/cm^2, but a large reduction of the threshold current from 183 mA down to 42 mA. However, previous work on THz QCL have shown, that the 1mm long, metal-metal waveguide devices, which were used as a reference, have negligible out-coupling losses since the large impedance mismatch between the waveguide and vacuum provides a reflectivity close above 75-80 % [24]. The fact that similar thresholds were observed in whispering gallery micro-cavity QCL fabricated with the same material corroborates this point [9]. As the active region is identical, the reduction of the threshold current density should be attributed to a reduction of the waveguide losses by the same amount.

In our metal-metal waveguide, the two components in-plane and perpendicular of the electric field vector generate losses of a different physical origin: the loss of the component normal to the layer will mainly be due to out of resonance intersubband absorption in the injector, the loss of the component in-plane to the layer originates from ohmic losses due to the free in-plane motion both in the active region as well as in the contact and metal layers.

#88988 - $15.00 USD Received 29 Oct 2007; revised 29 Nov 2007; accepted 29 Nov 2007; published 4 Dec 2007

The band structure of the injector may be optimized to minimize the amount of losses due to the normal component of the electric field, as shown in Ref. [26], we demonstrate here that the PBG structure may be used to reduce the loss originating from the in-plane component.

In the standing wave pattern of the laser mode, the maximum of the normal and in-plane components of the electric field are shifted by a quarter wavelength (see Annexe). In our PhC laser, thanks to the patterning of the active medium the anti-node of the in-plane field occurs in the low-index waveguide section (BCB), which, because it sustains a guided mode with a more rectangular profile, is intrinsically less lossy than the high-index section. This reduction of the losses is a unique feature of our deep etched, strongly confined PhC structure that was not present in previous QCL.

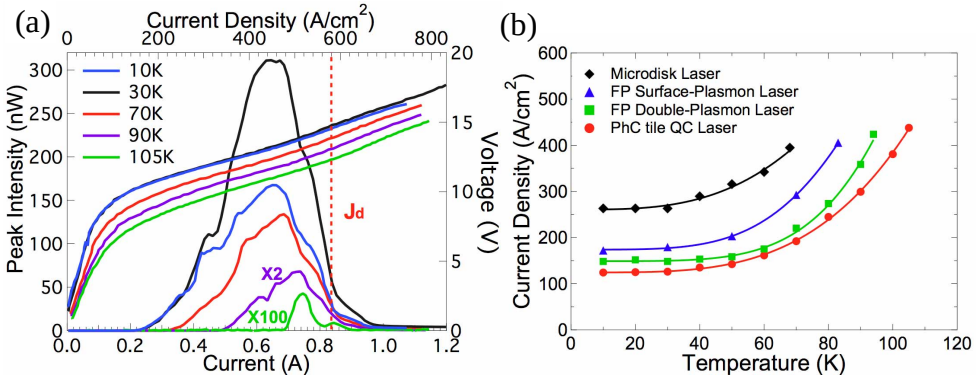

Fig. 4. L/I/V characterization of THz QCL PhC lasers as a function of temperature and the comparison of maximum operation temperature between different material systems. a, L/I/V characterization of peak intensity of the PhC tile laser at lattice parameter a=17 μm as a function of temperature under pulsed condition (pulse=200 ns, duty cycle=1.3%). The lowest threshold current density of this laser is 128 A/cm^2 and the maximum operation temperature is 105 K (intensities at 90 K and 105 K have been scaled by a factor of 2 and 100, respectively). Note that the value of the y scale does not describe the actual emitted power intensity, as the collection efficiency of the setup does not exceed 20%. b, Comparison of maximum operation temperature between PhC tile laser (600x600 μm^2, red circles), double plasmon FP ridge laser (1170x100 μm^2, green squares), surface plasmon FP ridge lasers (2000x200 μm^2, blue triangles) and micro-disk laser (50 μm radius, black circles). Continuous curves are guide for eye. All devices are processed from the same epilayer.

Figure 4(a) is the L/I/V measurement as a function of temperature. The a=17 μm PhC tile QCL operates up to 105 K under pulse condition. The dashed line at J_d =580 A/cm^2 represents the decay current density J_d for all the temperatures. Such L/I curve shape is caused by the energy mismatch between the material gain and the optical mode which limits the dynamic range.

There is a 17% improvement on the maximum operation temperature respect to the FP laser on the same layer. To further investigate the enhancement of temperature performance, we fit J_{th} versus temperature between PhC tile laser (600x600 μm^2), double plasmon FP ridge laser (1170x100 μm^2), surface plasmon FP ridge lasers (2000x200 μm^2) and micro-disk laser (50 μm radius), as shown in Fig. 4(b). Note that all of these lasers are fabricated with the same epilayer (N306). Based on its lowest current threshold density, our PhC tile QCL has the highest operating temperature among all the waveguides we were able to realize (and known in literature), including the best double plasmon FP laser with very comparable injected current, this indicates that exploiting PhC band engineering substantially enhances the gain, thus reduces the losses, and improves the temperature performance.

#88988 - $15.00 USD Received 29 Oct 2007; revised 29 Nov 2007; accepted 29 Nov 2007; published 4 Dec 2007

4. Conclusions

Our THz PhC tile QCLs combine optical dispersion engineering in PhCs and intersubband electronic engineering in QC structures. This is the first time PhC are successfully used to combine and enhance the key performances on THz QCLs over known FP and micro-disk lasers in all aspects. While remaining single mode, we have shown that employing PhCs allows a substantial reduction of the threshold current and current density due to slow light effects (or band-edge nature) of the lasing mode and we have simultaneously achieved a reduction in waveguide losses by exploiting the peculiarities of the PhC in a metal-metal waveguide. In the QC material used in the present study, a diagonal transition combined with a relatively weak coupling between the injector and the upper states allows a significant electrical tuning over a frequency range of 30 GHz. Such tuning range is achieved at a cost; the quantum design that enabled such a wide tuning due to the electrical tunability of the gain spectrum is inherently limited to lower operating temperatures. We believe that our approach, mixing PhC and metal-metal waveguide with designs adapted to higher operating temperatures [4] open the way toward low threshold, single mode and high operating temperature THz QCLs.

Acknowledgments

We thank Nicolas Hoyler and Marcella Giovannini for the MBE growth of the sample. This work was supported by the Swiss National Science Foundation and the National Center of Competence in Research, Quantum Photonics.

#88988 - $15.00 USD Received 29 Oct 2007; revised 29 Nov 2007; accepted 29 Nov 2007; published 4 Dec 2007

Annexes

I Fabrication

The epitaxial layer of the QCL is a repeated 120 periods of GaAs/$Al_{0.15}Ga_{0.85}As$ active layer growth by Molecular Beam Epitaxy (MBE) on a semi-insulating GaAs substrate. The lower surface-plasmon layer was formed by depositing a thick Au layer on the epitaxial layer. Successive thermocompression Au-Au bonding, polishing and selective wet etching completed the transfer of the epilayer onto an n^+ GaAs substrate. The PhC laser pattern was defined by photolithography using AZ5214 photoresist, and then transferred into the 900 nm SiO_x hard mask using a CHF_3 based plasma mixture in Reactive Ion Etching (RIE). The epitaxial QCL structure was etched down through the entire active region to the Au layer (15.5 μm) using a Cl_2 based chemistry RIE. In order to obtain uniform current injection of the unconnected pillars we developed a multilayer BCB planarization technique on the deeply etched structures, which enables lithographic deposition of top metal contacts. To ensure that all the pillar tops are accessible for contacting, the BCB was etched up to 800 nm lower than the pillar tops with CF_4 based plasma mixture. The upper surface plasmon layer which acts also as top contact was lithographically patterned using TI35ES negative photoresist with 3.5 μm thick undercut profile, followed by Ti/Au (5/1800 nm) evaporation and lift-off. The bottom contact, constituted by a Ti/Au (5/500 nm) layer, was deposited on the backside of the GaAs n^+ substrate. The samples were cleaved, mounted on copper heatsinks and wire bonded with 25 μm diameter gold wires.

II Measurement

The lasing spectra and Electro-Luminescence (EL) spectra measurements, and light-current-voltage (L/I/V) curves against temperature in both pulsed and Continuous-Wave (CW) conditions were performed using a home-built, under-vacuum Fourier-Transform-Infra-Red (FTIR) spectrometer equipped with a He-cooled bolometer. Spectral measurements were performed with a step scan and lock-in technique: the maximum resolution of such system is 0.03 meV.

III Waveguide losses

Let us assume for simplicity a metal-metal waveguide in which a TM mode is propagating in the y direction; z is the confinement direction. The magnetic induction will then have the dependence given by:

$$\vec{B} = (B_x(z)e^{i(\beta y - \omega t)}, 0, 0) \tag{1}$$

where β is the propagation constant, ω the light angular frequency and $B_x(z)$ the z dependence of the B-field. The time derivative of two components (y and z) of the electric field may be derived from the magnetic field vector using:

$$\nabla \times \vec{B} = \varepsilon\mu_0 \frac{\partial}{\partial t}\vec{E} \tag{2}$$

and therefore we have:

$$E_z(z) = -\frac{\beta}{\omega\varepsilon\mu_0} B_x(z)e^{i(\beta y - \omega t)} \tag{3}$$

and

$$E_y(z) = \frac{i}{\omega\varepsilon\mu_0}\frac{\partial}{\partial z} B_x(z)e^{i(\beta y - \omega t)} \tag{4}$$

#88988 - $15.00 USD Received 29 Oct 2007; revised 29 Nov 2007; accepted 29 Nov 2007; published 4 Dec 2007

As shown by Eq. (3) and Eq. (4), the two components of the electric field exhibit a $\pi/2$ phase shift in respect to each other; the standing wave pattern produced by two such counter-propagating fields will therefore producing standing waves shifted by a quarter wavelength.

#88988 - $15.00 USD Received 29 Oct 2007; revised 29 Nov 2007; accepted 29 Nov 2007; published 4 Dec 2007